



# Structural characterization and property modification for two-dimensional (001) SrTiO<sub>3</sub> nanosheets

Yuanbin Xue<sup>1</sup> · Cuihuan Geng<sup>1</sup> · Yao Guo<sup>1</sup>

Received: 11 June 2020 / Accepted: 30 July 2020 / Published online: 9 August 2020  
© King Abdulaziz City for Science and Technology 2020

## Abstract

The recent success in fabrication of free-standing perovskite oxide films, the thickness of which can be controlled at the atomic scale, breaks new ground in pursuing advanced low-dimensional materials. In this work, the structural characteristics and property modification of 2D (001) SrTiO<sub>3</sub> nanosheets were investigated theoretically. Our results unveil that the system is subject to significant differentiation of Ti–O bonds and several competing structural phases; the properties are layer-dependent, and functionalities are more likely to emerge near the surface; the bandgap can be effectively adjusted by strain, but the in-plane strain has the opposite effect to the out-of-plane strain; electron-doping by V brings about magnetism without breaking the semiconductor nature while hole-doping by Al makes the system exhibit metallic and complex magnetic features. Our findings could partly explain the experimentally observed unusual flexibility and may be also useful to facilitate the understanding of 2D perovskite-based materials.

**Keywords** Layer-dependent properties · Antiferro-distortion · Metallicity · Magnetism · Theoretical calculation

## Introduction

Current scientific interest in the search for promising low-dimensional materials shows no signs of ceasing to grow (Xiao and Liu 2019; Zhao et al. 2018). Since graphite was exfoliated into graphene (Novoselov et al. 2004), 2D materials have emerged as a new frontier in this field due to many unique advantages they have (Zhou et al. 2019), such as interesting electronic, magnetic, mechanical and optical properties (Novoselov et al. 2016; Tan et al. 2017; Xiao et al. 2012; Ren et al. 2015). Nowadays almost all traditional 2D materials have van der Waals layered structures and their membranes can be easily made from the parent bulk crystals (Birkhölzer and Koster 2019). However, this does not apply to those with strongly bound three-dimensional (3D) lattices,

such as technologically useful perovskite oxides (Birkhölzer and Koster 2019). Perovskite oxides display a rich variety of useful physical effects which result from electron–electron correlations among the constituent transition-metal ions (Imada et al. 1998). However, the investigations of them have long been confined in epitaxial films grown on top of a substrate.

Fortunately, Lu et al. (2016) developed a common method to prepare free-standing ultrathin perovskite films, and using it Ji et al. (2019) gave the first experimental evidence on the existence of free-standing monolayer perovskite films. Soon after, ferroelectric domain transition was observed in 2D PbTiO<sub>3</sub> (PTO) under giant uniaxial tensile strain condition (Han et al. 2020). On the theoretical side, some other stable perovskite monolayers were proposed (Xiao and Liu 2019) and adjustable electric and magnetic properties were predicted in 2D LaAlO<sub>3</sub>/SrTiO<sub>3</sub> heterostructures (Xue et al. 2020). However, compared to the traditional layered 2D materials, the knowledge of non-layered 2D materials in the perovskite system is still very limited and inconclusive, and we expect that one of the progress in this field is to explore or design new properties in the non-layered 2D perovskite films to make them competitive with other 2D materials.

Therefore, in this work much effort has been devoted to theoretically study the atomic and electronic properties of

**Electronic supplementary material** The online version of this article (<https://doi.org/10.1007/s13204-020-01528-2>) contains supplementary material, which is available to authorized users.

✉ Yao Guo  
guoyao@ayit.edu.cn

<sup>1</sup> Henan Joint International Research Laboratory of Nanocomposite Sensing Materials, Department of Chemical and Environmental Engineering, Anyang Institute of Technology, Anyang 455000, China

a series of 2D (001) STO nanosheets and we also reported the effect of strain and doping (with Al and V element) on the systems. The main objective in this study is to explore the structure–function relationship in 2D STO and look for effective ways to tune the system properties.

### Computational and structural modeling details

All calculations were carried out using the Vienna Ab initio Simulation Package (VASP) (Kresse and Furthmüller 1996a, b). The projector-augmented wave (PAW) (Blochl 1994; Kresse and Joubert 1999) method was used to describe the ion–electron interaction. The exchange correlation between electrons was treated by the generalized gradient approximation (GGA) of Perdew–Burke–Ernzerhof (PBE) (Perdew et al. 1996) plus the on-site Coulomb interaction approach, with  $U_{\text{eff}} = 4.36$  eV (Wang et al. 2010; Li et al. 2017) and 5.29 eV (Casula et al. 2012; Li et al. 2017) for Ti 3d and V 3d orbitals, respectively. The cutoff kinetic energy was set at 450 eV. The electronic self-consistent loop and the ionic relaxation loop converged to  $10^{-5}$  eV and  $0.02$  eV  $\text{\AA}^{-1}$ , respectively. Dipole correction (Bengtsson 1999) and a vacuum layer of over 15  $\text{\AA}$  were applied. The 2D (001) STO nanosheets with thickness from 1 to 3 unit cells (u.c.) were simulated. To explicitly model the oxygen octahedron rotation, supercells with  $(2 \times 2)$  in-plane dimension were used. The simulations of doped systems were performed in larger

supercells with  $(2\sqrt{2} \times 2\sqrt{2})$  dimension. For supercells with  $(2 \times 2)$  in-plane dimension, the Brillouin zone was sampled with a  $3 \times 3 \times 1$  Monkhorst–Pack (Monkhorst and Pack 1976)  $k$ -point mesh for ionic relaxation and a denser  $6 \times 6 \times 1$  Gamma-centered mesh for static calculations, respectively. For supercells with  $(2\sqrt{2} \times 2\sqrt{2})$  in-plane dimension, the corresponding  $k$  grids are  $2 \times 2 \times 1$  Monkhorst–Pack mesh and  $4 \times 4 \times 1$  Gamma-centered mesh, respectively.

## Results and discussion

### Changes in atomic structure of 2D STO as compared to 3D STO

The calculated in-plane lattice parameters are 3.901  $\text{\AA}$ , 3.924  $\text{\AA}$ , and 3.932  $\text{\AA}$  for 1-, 2- and 3-u.c. thick STO sheets, respectively. Compared to the theoretical bulk value (3.965  $\text{\AA}$ ), these data mean that the 2D (001) STO nanosheets shrink by about 0.8–1.6% in their lateral dimension. The relaxed atomic structures remain nearly the same as in the bulk, especially for the thicker cases, but closer inspection reveals that rumpling of ions came about; see Fig. 1a for examples. The anions and cations show  $z$ -axis oriented relative displacement, e.g. the O and Ti ions are no longer on the same horizontal plane. The rearrangement of ions

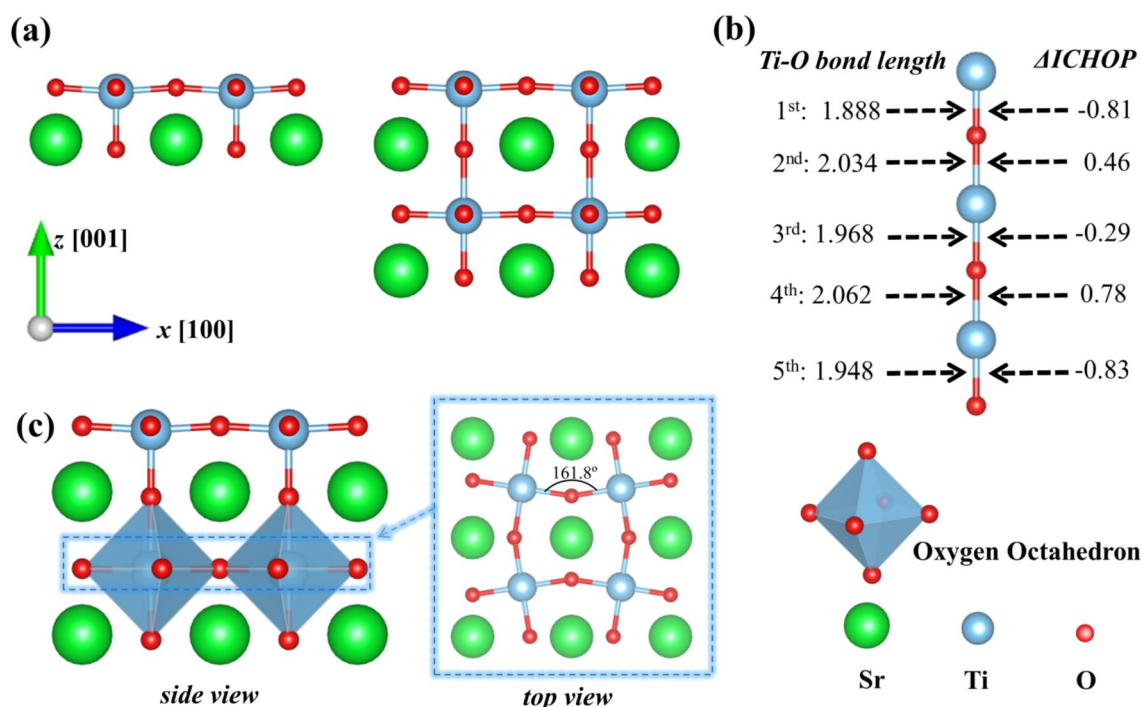


**Fig. 1** **a** Relaxed structures of 1- and 2-u.c. thick 2D STO. **b** The bond length and relative ICOHP of each Ti–O bond along [001] direction in 3-u.c. thick STO. **c** Relaxed structures of 2-u.c. thick STO with AFD configuration

was further confirmed by their bond lengths summarized in Table S1. In general, Ti–O bonds are in the range of about 1.90 to 2.05 Å and the Sr–O bond lengths fall into the scope of about 2.60 to 2.90 Å.

As is well known, the bond strength is usually closely associated with the bond length, and the change in the latter may well reflect a change in the former. To quantitatively analyze the interatomic interactions, we calculated the integrated crystal Hamilton population (ICOHP) (Dronskowski and Bloechl 1993; Deringer et al. 2011), which can be regarded as a bond strength indicator (the smaller the ICOHP, the stronger the bond strength). By making statistics of ICOHP, given in Table S1, we have three major findings. First, as a whole, the Sr–O interactions do not change very much (within 0.1 eV) while the Ti–O interactions vary significantly (over 1 eV in some cases). Second, the in-plane Ti–O bonds have similar ICOHP to those of bulk STO. Third, the Ti–O interactions along the out-of-plane direction fluctuate most (differ by over 1 eV in many cases), implying that some Ti–O pairs dimerized while the others decoupled.

Further analysis showed that the out-of-plane Ti–O bonds can be roughly divided into two groups: the strengthened one and the weakened one. Presented in Fig. 1b is an example to display the  $z$ -dependent bond length and the ICOHP relative to the bulk value ( $\Delta$ ICOHP). Figure 1b not only clearly displays that the stronger Ti–O bonds and the weaker Ti–O bonds have an alternating arrangement but also demonstrates that the strengthened Ti–O bonds have shorter bond length while the weakened Ti–O bonds have longer bond length. Moreover, data in Table S1 show that no matter what the film thickness is, the Ti–O bonds nearest to the surface have the lowest ICOHP (highest bond strength).

In addition to ordinary atomic relaxation and rumpling, perovskite films may also undergo antiferro-distortion (AFD), i.e. one oxygen octahedron rotates clockwise and the nearest neighboring one rotates counterclockwise), which was found to be strong in epitaxially grown thin perovskite films (Fong et al. 2004; Munkholm et al. 2002). We infer that the AFD phase transition is more likely to take place in free-standing 2D STO nanosheets due to the lack of substrate-caused constraint. In this work, both  $z$ -oriented AFD phase (i.e. oxygen octahedrons rotate around  $z$ -axis) and  $y$ -oriented AFD phase (i.e. oxygen octahedrons rotate around  $y$ -axis) were taken into consideration. As  $x$ -oriented AFD phase is equivalent to the  $y$ -oriented one due to symmetric restriction, it was not investigated explicitly.

To trigger AFD phase, we manually rotated the oxygen octahedrons by a small angle (within  $3^\circ$ ) before structural optimization. After calculation, AFD seems stable for the 2- and 3-u.c. thick films, see Fig. 1c, but we were not able to stabilize the distorted 1-u.c thick nanosheet. Besides, in the  $z$ -oriented AFD phase the  $\text{TiO}_5$  units on the surfaces restored to be undistorted. However, they could maintain

rotated in the  $y$ -oriented AFD phase, as shown in Fig. S1. As for the lattice constants, AFD phase transition only has a marginal effect on them. It is worth mentioning that in the epitaxial PTO films grown on STO substrate, AFD structures were also observed before (Munkholm et al. 2002), and they were thought to be responsible for the system stability and the occurrence of in-plane polarization. But that AFD phase appeared only near the PTO surface region, which might be explained by the restrictive epitaxial strain resulting from the substrate. Very recently, it was reported that the competitive relationship between the AFD and ferroelectricity in 2D freestanding  $\text{BaTiO}_3/\text{SrTiO}_3$  heterostructures is one of the reasons for the weak in-plane polarization (Jia et al. 2020).

It was also found that AFD phase transition gave rise to further change in atomic structures. First, the Ti–O–Ti bond angle changed most. For example, in the 2-u.c. thick model the in-plane Ti–O–Ti bond angle changed from  $180^\circ$  to about  $162^\circ$ ; see Fig. 1c. Moreover, the bond lengths changed as well, and the values are summarized in Table S2 and Table S3, which demonstrate that it is the Sr–O bond length that fluctuates dramatically, ranging from about 2.60 to 3.10 Å. Another striking feature is that although Sr–O bond length changed very much, their bond strength did not. The relative ICOHP values in Table S2 and Table S3 reflect the bond strength variation induced by  $z$ -oriented and  $y$ -oriented AFD, respectively. There is no statistically significant difference in these two sets of data, indicating that the  $z$ -oriented and  $y$ -oriented rotation modes have a similar effect on the bond strength in 2D (001) STO.

Unexpectedly, although the Ti–O–Ti bond chains deformed severely, the system energy only changed slightly, about 10 meV/u.c.; see Table 1. This implies that 2D (001) STO are subject to several competing structural phases and their bonds tend to be bent, which might give them a strong capacity to accommodate the structural distortion. Previous experiment discovered that STO, although brittle in bulk form, becomes flexible at a thickness of a few unit cells and can be even folded (Ji et al. 2019). Based on our results, we may conclude that the fluctuations near these energy-close phases are responsible, to some extent, for the unusual flexibility observed in the experiment.

**Table 1** The energy change (eV/u.c.) in 2D STO with different thickness after the introduction of antiferro-distortion

Rotation Mode	2-u.c. thick STO	3-u.c. thick STO
mode- $z$	−0.010	−0.012
mode- $y$	0.001	−0.013

The  $z$ -oriented AFD phase and  $y$ -oriented AFD phase are represented by mode- $z$  and mode- $y$ , respectively

## Electronic structures

In this section, we will discuss the electronic properties of 2D (001) STO. First comes the band structures. It was found that all of the 1-, 2- and 3-u.c. thick STO nanosheets are semiconductors with an indirect bandgap of about 2.29, 1.59 and 1.47 eV, respectively. No matter whether the AFD phase exists or not, the conduction-band minimum (CBM) is at the  $\Gamma$  point while the valence-band maximum (VBM) at the M point, as shown in Fig. S2. The bandgap changed a little (within 0.1 eV) after the introduction of the AFD phase.

As the VBM and CBM electronic states predominantly influence the functionalities of semiconductor materials, it is natural to further probe their properties. To locate where the VBM and CBM electrons are, we show their spatial distribution in Fig. 2, which displays that the VBM electrons are almost located on the topmost Ti–O layer while the CBM electrons primarily lie on the bottom Ti–O layer. This gives the evidence that the electronic properties of 2D (001) STO are not uniform, but layer-dependent. Besides, the partial density of states (pDOS) in Fig. S3 further shows that it is the O  $2p_x+2p_y$  orbitals that accommodate the VBM

electrons while the CBM electrons populate the  $3d_{xy}$  orbitals of Ti element. The orbital occupation is similar to the case of bulk STO (Shanthi and Sarma 1998; Marel et al. 2011), but the VBM and CBM electrons are uniformly distributed on each Ti–O layer in bulk STO. Still, we found that these conclusions apply to those structures with AFD.

## The response to strain

It is also important to figure out how 2D STO nanosheets respond to an external stimulus, for this issue is closely connected to their practical uses. Here, we chose strain as the study object, which is the common and facile strategy for manipulating the material properties (Xue et al. 2020; Huang et al. 2019; Han et al. 2020). Both in-plane and out-of-plane strains were considered for the purpose of comparison.

We first investigated the impact of strain on the atomic structures. On the one hand, the compressive (tensile) in-plane strain is beneficial to (goes against) the  $z$ -oriented AFD. The Ti–O–Ti angle in 2-u.c. thick STO was able to bend further to  $154.5^\circ$  under about 3% compressive in-plane strain while it nearly restored to  $172.3^\circ$  when about

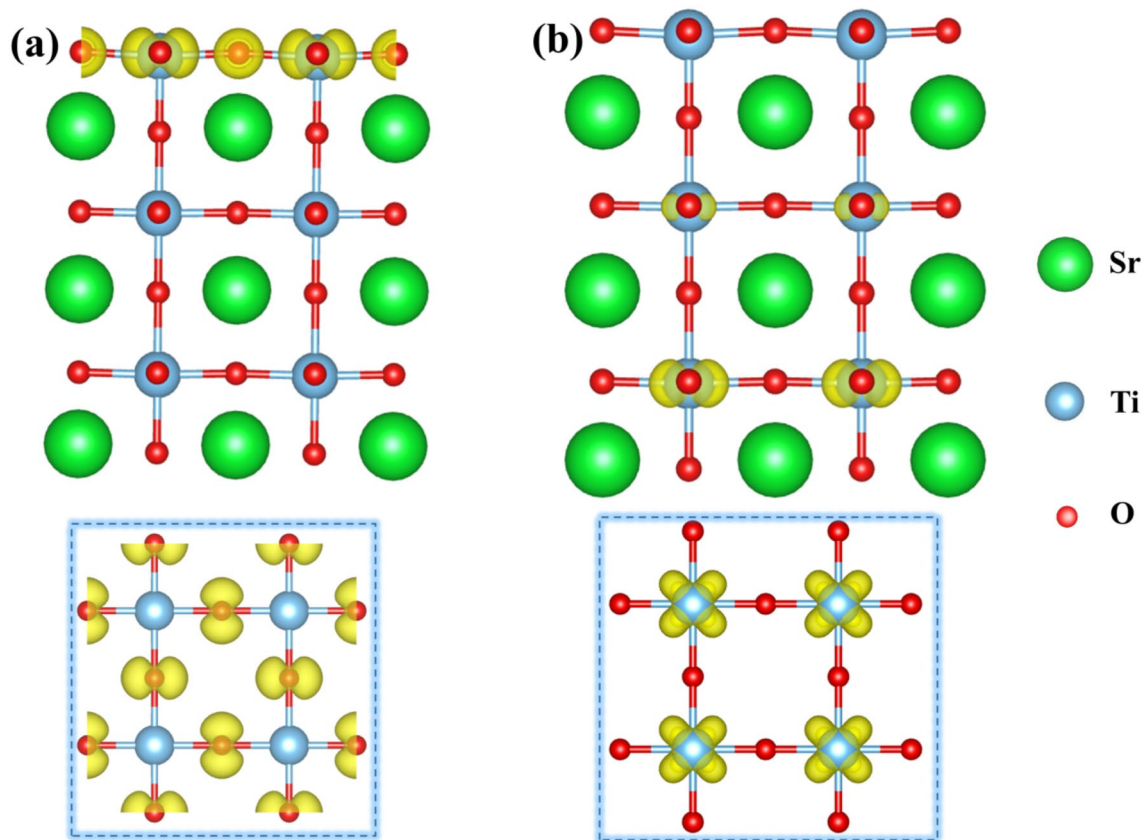


**Fig. 2** The distribution of electrons with energy close (within 0.2 eV) to **a** VBM and **b** CBM in 2-u.c. thick STO sheet. The top views of the uppermost Ti–O layer and the lowest Ti–O layer are also presented at

the bottom of **(a, b)**, respectively. All isosurfaces are visualized with VESTA code (Momma and Izumi 2008) and the isovalues are set at 0.001

3% tensile in-plane was applied; see Fig. S4a, b. By contrast, compressive (tensile) in-plane strain goes against (is beneficial to) the  $y$ -oriented AFD. For instance, this type of distortion in 2-u.c. thick STO was weaker or nearly absent under about 2% compressive in-plane strain while it became severer when undergoing about 3% tensile in-plane strain; see Fig. S4c, d. On the other hand, the out-of-plane strain has a relatively weaker effect on the  $z$ -oriented rotation. Within the entire strain range under investigation ( $-5$  to  $+5\%$ ), the  $z$ -oriented rotation could remain. However, the  $y$ -oriented rotation could be enhanced by the compressive out-of-plane strain, but severely suppressed by the tensile out-of-plane strain.

The influence of strain on the bandgap can be summarized as follows. The compressive in-plane strain decreases the bandgap while the tensile in-plane strain shows the opposite effect. In the strain range studied ( $-5$  to  $+5\%$ ), the bandgap falls into 1.99–2.35 eV, 1.34–1.81 eV and 1.19–1.72 eV for the 1-, 2- and 3-u.c. thick STO sheets, respectively, which means that the bandgap changes by about  $-13$  to  $3\%$ ,  $-16$  to  $14\%$  and  $-20$  to  $17\%$ , respectively, compared to the unstrained counterparts. By contrast, the compressive out-of-plane strain increases the bandgap while the tensile out-of-plane strain decreases the bandgap. When the strain changes from  $-5$  to  $+5\%$ , the bandgap changes from 2.44 to 2.15 eV, 1.75 to 1.41 eV and 1.66 to 1.26 eV for the 1-, 2- and 3-u.c. thick STO sheets, respectively. The corresponding amplitude of variation is about  $7$  to  $-6\%$ ,  $11$  to  $-11\%$  and  $13$  to  $-14\%$ , respectively. The features of bandgap as a function of strain are captured in Fig. 3. This picture also indicates that the band gaps of 2D (001) STO with different thickness share nearly the same trend as the strain varies. Moreover, it can be seen from Fig. 3 that the effect of strain on bandgap seems to be orientation-dependent. The possible

reason is that the  $z$ -lattice parameter (the lattice parameter along the out-of-plane direction) varies differently under different strain conditions. To be specific, when in-plane compressive (tensile) strain is applied it increases (decreases), while it decreases (increases) when out-of-plane compressive (tensile) strain is applied. We found that the bandgap becomes larger when the  $z$ -lattice parameter decreases while it becomes smaller when the  $z$ -lattice parameter increases.

### The effect of electron- and hole-doping

In the preceding part, we have discussed the properties of pure 2D STO, which is an ordinary nonmagnetic semiconductor with an indirect bandgap. To achieve new or improved properties, one of the common practices is doping design. Here both electron- and hole-doping were explored and they were realized by ion substitution (with V and Al) for Ti.

Some interesting findings about the electronic properties emerged after the systems were doped. On the one hand, although V atom could donate one extra electron, V-doped 2D STO remained semi-conductive, and this is supported by the DOS plots in Fig. S5. However, electron-doping by V brought about magnetism and the total magnetic moment was around  $1 \mu_B$  no matter the dopant was on the surficial or inner Ti–O layer. Figure 4a displays the magnetic density distribution in 3-u.c. thick STO, indicating that the magnetic charges are predominantly localized on V atom. We also discovered that the semi-conductive and magnetic states can persist after the introduction of the AFD phase.

On the other hand, when hole-doped by Al, the system turned to be metallic; see Fig. S6. However, the Al-doped 2D (001) STO without AFD are in non-magnetic state, but magnetism (with the total magnetic moment being about 0.5

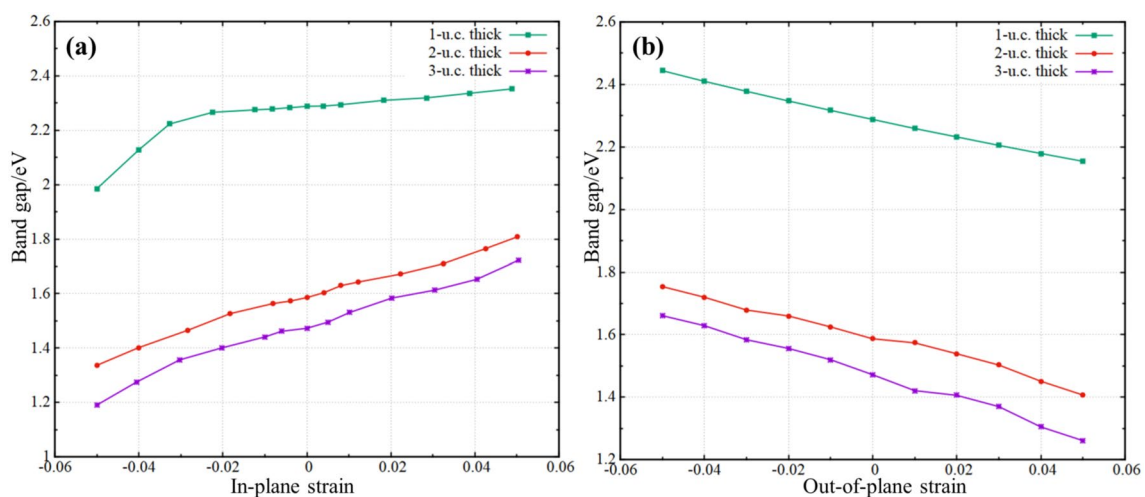


**Fig. 3** Bandgap of 2D (001) STO nanosheets with different thicknesses as a function of **a** in-plane strain and **b** out-of-plane strain. The positive numbers on the horizontal axis represent tensile strain while the negative ones stand for compressive strain

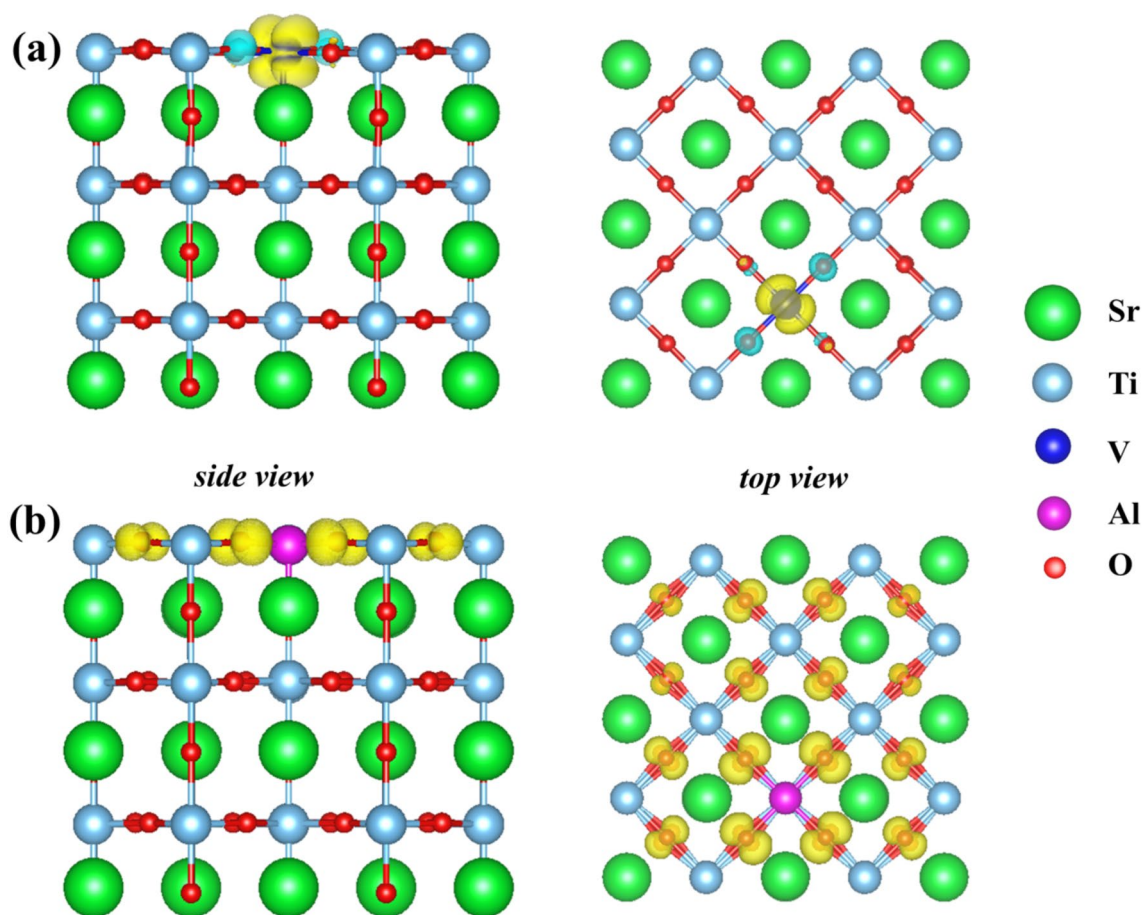


**Fig. 4** The magnetic density distribution profiles for **a** V-doped and **b** Al-doped STO nanosheets. Both side view (left) and top view (right) are given. The isovalues are set at 0.004 and 0.001 for (a, b), respectively

$\mu_B$ ) could occur at the presence of AFD, especially when Al is on the surficial Ti–O layer; see Fig. 4b. These discoveries imply that the magnetic state of Al-doped 2D STO is more sensitive to the atomic structure. The net magnetic moments are derived from O  $2p$  orbitals, not the common  $d$  orbitals of a transition metal ion, and the magnetic electrons are delocalized on almost the whole top Ti–O layer. Therefore, the magnetism and conductivity of Al-doped 2D STO nearly result from the same O atoms, implying the coupling between magnetism and conductivity.

## Conclusions

In summary, using first-principles calculations, we have systematically studied the structural properties of 2D (001) STO nanosheets and explored the ways to modifying their physics. First, we discovered the alternating arrangement of strengthened and weakened Ti–O bonds along the out-of-plane direction. In addition, 2D STO is subject to several competing structural phases induced by oxygen octahedron

rotation. These competing phases slightly influence the system energy, which is consistent with the experimentally observed unusual flexibility of 2D STO (Ji et al. 2019). Second, layer-dependent properties were found. The VBM and CBM electronic states do not uniformly distribute on each (001) layer, but preferentially located on the surficial region, which may give rise to unique properties. Last, we suggest that both strain engineering and doping are effective strategies to tailor the properties of 2D STO, such as the modification of bandgap and the introduction of metallicity or magnetism.

**Acknowledgments** The authors acknowledge the support from the Henan Joint International Research Laboratory of Nanocomposite Sensing Materials, the National Natural Science Foundation of China (No. 21971155) and the Key Research Project of He'nan Provincial Higher Education (No. 20A430002 and No. 20B150001).

## Compliance with ethical standards

**Conflict of interest** On behalf of all authors, the corresponding author states that there is no conflict of interest.

## References

- Bengtsson L (1999) Dipole correction for surface supercell calculations. *Phys Rev B* 59:12301–12304
- Birkhölzer Y, Koster G (2019) How to make the thinnest possible freestanding sheets of perovskite materials. *Nature* 570:39–40
- Bloch PE (1994) Projector augmented wave method. *Phys Rev B* 50:17953–17979
- Casula M, Werner P, Vaugier L, Aryasetiawan F, Miyake T, Millis AJ, Biermann S (2012) Low-energy models for correlated materials: bandwidth renormalization from coulombic screening. *Phys Rev Lett* 109:126408
- Deringer VL, Tchougreff AL, Dronskowski R (2011) Crystal Orbital Hamilton Population (COHP) analysis as projected from plane-wave basis sets. *J Phys Chem A* 115:5461–5466
- Dronskowski R, Blochl PE (1993) Crystal Orbital Hamilton Populations (COHP): energy-resolved visualization of chemical bonding in solids based on density-functional calculations. *J Phys Chem* 97:8617–8624
- Fong DD, Stephenson GB, Streiffer SK, Eastman JA, Auciello O, Fuoss PH, Thompson C (2004) Ferroelectricity in ultrathin perovskite films. *Science* 304:1650–1653
- Han L, Fang Y, Zhao Y, Zang Y, Gu Z, Nie Y, Pan X (2020) Giant uniaxial strain ferroelectric domain tuning in freestanding  $\text{PbTiO}_3$  films. *Adv Mater Interfaces* 7:1901604
- Huang T, Wei W, Chen X, Dai N (2019) Strained 2D layered materials and heterojunctions. *Ann Phys* 531:1800465
- Imada M, Fujimori A, Tokura Y (1998) Metal-insulator transitions. *Rev Mod Phys* 70:1039–1263
- Ji D, Cai S, Paudel TR, Sun H, Zhang C, Han L, Wei Y, Zang Y, Gu M, Zhang Y, Gao W, Huan H, Guo W, Wu D, Gu Z, Tsymbal EY, Wang P, Nie Y, Pan X (2019) Freestanding crystalline oxide perovskites down to the monolayer limit. *Nature* 570:87–90
- Jia F, Xu S, Zhao G, Liu C, Ren W (2020) Structural and electronic properties of two-dimensional freestanding  $\text{BaTiO}_3/\text{SrTiO}_3$  heterostructures. *Phys Rev B*. 101:144106
- Kresse G, Furthmüller J (1996a) Efficiency of ab initio total energy calculations for metals and semiconductors using a plane-wave basis set. *Comput Mater Sci* 6:15–50
- Kresse G, Furthmüller J (1996b) Efficient iterative schemes for ab initio total-energy calculations using a plane-wave basis set. *Phys Rev B* 54:11169–11186
- Kresse G, Joubert D (1999) From ultrasoft pseudopotentials to the projector augmented-wave method. *Phys Rev B* 59:1758–1775
- Li J, Yin D, Li Q, Sun R, Huang S, Meng F (2017) Interfacial defects induced electronic property transformation at perovskite  $\text{SrVO}_3/\text{SrTiO}_3$  and  $\text{LaCrO}_3/\text{SrTiO}_3$  heterointerfaces. *Phys Chem Chem Phys* 19:6945–6951
- Lu D, Baek DJ, Hong SS, Kourkoutis LF, Hikita Y, Hwang HY (2016) Synthesis of freestanding single-crystal perovskite films and heterostructures by etching of sacrificial water-soluble layers. *Nat Mater* 15:1255–1260
- Marel D, van Mechelen D, Mazin I (2011) Common Fermi-liquid origin of  $T^2$  resistivity and superconductivity in *n*-type  $\text{SrTiO}_3$ . *Phys Rev B* 84:205111
- Momma K, Izumi F (2008) VESTA: a three-dimensional visualization system for electronic and structural analysis. *J Appl Crystallogr* 41:653–658
- Monkhorst HJ, Pack JD (1976) Special points for Brillouin-zone integrations. *Phys Rev B* 13:5188–5192
- Munkholm A, Streiffer S, Murty R, Eastman J, Thompson C, Auciello O, Thompson L, Moore J, Stephenson G (2002) Antiferrodistortive reconstruction of the  $\text{PbTiO}_3$  (001) surface. *Phys Rev Lett* 88:016101
- Novoselov KS, Geim AK, Morozov SV, Jiang D, Zhang Y, Dubonos SV, Grigorieva IV, Firsov AA (2004) Electric field effect in atomically thin carbon films. *Science* 306:666–669
- Novoselov K, Mishchenko A, Carvalho A, Castro-Neto A (2016) 2D materials and van der Waals heterostructures. *Science* 353:aac9439
- Perdew JP, Burke K, Ernzerhof M (1996) Generalized gradient approximation made simple. *Phys Rev Lett* 77:3865–3868
- Ren YF, Qiao ZH, Niu Q (2015) Topological phases in two-dimensional materials: a brief review. *Rep Prog Phys*, p 79
- Shanthi N, Sarma DD (1998) Electronic structure of electron doped  $\text{SrTiO}_3$ :  $\text{SrTiO}_{3-\delta}$  and  $\text{Sr}_{1-x}\text{La}_x\text{TiO}_3$ . *Phys Rev B* 57:2153–2158
- Tan C, Cao X, Wu X-J, He Q, Yang J, Zhang X, Junze C, Zhao W, Han S, Nam G-H, Sindoro M, Zhang H (2017) Recent advances in ultrathin two-dimensional nanomaterials. *Chem Rev* 117:6225–6331
- Wang Z, Okude M, Saito M, Tsukimoto S, Ohtomo A, Tsukada M, Kawasaki M, Ikuhara Y (2010) Dimensionality-driven insulator-metal transition in a-site excess non-stoichiometric perovskites. *Nat Commun* 1:106
- Xiao X-B, Liu B-G (2019) Stable structures and electronic properties of perovskite oxide monolayers. [arXiv:1907.00898](https://arxiv.org/abs/1907.00898)
- Xiao D, Liu G-B, Feng W, Xu X, Yao W (2012) Coupled spin and valley physics in monolayers of  $\text{MoS}_2$  and other group-VI dichalcogenides. *Phys Rev Lett* 108:196802
- Xue Y, Geng C, Guo Y (2020) Two-dimensional (001)  $\text{LaAlO}_3/\text{SrTiO}_3$  heterostructures with adjustable band gap and magnetic properties. *ACS Appl Mater Interfaces* 12:3134–3139
- Zhao Y, Lin L, Zhou Q, Li Y, Yuan S, Chen Q, Dong S, Wang J (2018) Surface vacancy-induced switchable electric polarization and enhanced ferromagnetism in monolayer metal trihalides. *Nano Lett* 18:2943–2949
- Zhou N, Yang R, Zhai T (2019) Two-dimensional non-layered materials. *Mater Today Nano* 8:100051

**Publisher's Note** Springer Nature remains neutral with regard to jurisdictional claims in published maps and institutional affiliations.